• Multimodal Analysis of Saddle Micro-terrain Prone to Wind Disasters on Overhead Transmission Lines

Ying Deng[1], Xingliang Jiang [1], Hongxia Wang[2], Yang Yang[2],Muhammad Shakeel Virk[3], Yi Liao[1], Jianguo Wu[1], Mingguan Zhao[2]

[1] Xuefeng Mountain Energy Equipment Safety National Observation and Research Station of Chongqing University, Chongqing University, Chongqing, 400044, China

[2] Power Research Institute of State Grid Xinjiang Electric Power Co.

[3] Arctic Technology & Icing Research Group, UiT – The Arctic University of Norway 8505 Narvik, Norway

yingdeng@cqu.edu.cn, xljiang@cqu.edu.cn, wanghongxiaab@163.com, 17799770176@163.com, muhammad.s.virk@uit.no, liaoyi@cqu.edu.cn, jianguowu@cqu.edu.cn, 1847285896@qq.com

Abstract

Pervasive micro-terrain is a significant contributor to wind disasters on transmission lines. This study explores the effect of saddle micro-terrain on the wind field of transmission lines and proposes relevant models and analysis methods. Firstly, the characteristic elements and parameters of saddle micro-terrain are extracted using DEM and established representative cross-sections for classification. Subsequently, a multimodal computational model is developed, considering the geographical and meteorological features and the sag model of transmission lines under micro-terrain. This study calculates wind field distribution and conductor wind loads for three types of saddle micro-terrain conditions, revealing an exponential growth trend of wind loads with increasing wind speeds. The results indicate that in transmission lines at saddle areas, the sag region does not intrude into the boundary layer, with a wind speed growth rate of only 0.18, resulting in relatively stable wind loads. In contrast, for transmission lines at saddle areas in secondary mountain ranges and dual-mountain saddle regions, wind speed growth rates reach 0.97 and 1.53, respectively, indicating higher disaster risks. This research provides a basis for distinguishing and disaster prevention in mountainous transmission lines' micro-terrain variations, offering significant contributions to enhancing wind-resistant design standards in mountainous regions.

Keywords—Transmission line; Micro-terrain; DEM; Multimodal analysis; Wind lord

* Corresponding author. Xuefeng Mountain Energy Equipment Safety National Observation and Research Station of Chongqing University. Tel.: +86 199 3607 5658.

E-mail address: yingdeng@cqu.edu.cn.

Nomenclature

Acronyms		**Variables**	
DEM	Digital Elevation Model	$\{\bar{F}\}_e$	The force vector array of unit conductor nodes.
UHV	Ultra-high Voltage	$\{\bar{\delta}\}_e$	The displacement vector array of unit conductor nodes.
GIS	Geographic Information Systems	$[\bar{K}]_e$	The stiffness matrix of a unit conductor.
CFD	computational fluid dynamics	$U(z)$	The wind speed at z height of the mountain
LES	Large-eddy simulations	$U_0(z)$	The wind speed at z height of the flat land.
ASF	Alaska Satellite Facility	$k(z)$	The profile of turbulent kinetic energy
DAAC	Distributed Active Archive Centers	$\varepsilon(z)$	The profile of dissipation rate
LGJ	Steel Core Aluminum Stranded Wire	$I(z)$	The turbulence degree
CQU	Chongqing University	S	The acceleration ratio
HFFB	High-frequency force balance	I	The turbulence intensity
Parameters			
□H_a	The vertical projection distance from the horizontal plane to the feature point a	l	The projected length of L on the horizontal plane
□H_b	The vertical projection distance from the horizontal plane to the feature point b	W	The inter-mountain distance
□h	The vertical projection distance from the horizontal plane to the saddle point P	γ	The angle of the mountain flank uplift
R_1	The horizontal projection distance between the saddle point P and the feature point a	[T]	The coordinate transformation matrix
R_2	The horizontal projection distance between the saddle point P and the feature point b	C_u	The empirical constant
$\tan\alpha$	The ratio of slope between the saddle point P and the feature point a	K	The Carmen constant
$\tan\beta$	The ratio of slope between the saddle point P and the feature point b	L_u	The turbulence integration scale
H	The height of the mountain	E	The Young's modulus
D	The diameter of the mountain	A	The cross-sectional area of the conductor
L	The length of the ridgeline	l_{ij}	The unit conductor length

1 Introduction

As China's power grids continue to expand, the "14th Five-Year Plan" period prioritizes the development of ultra-high voltage transmission lines and new energy generation. The proper site selection plays a crucial role in facilitating long-distance UHV transmission and wind power generation [1-3]. However, these developments will traverse areas with complex topography and variable climate conditions [4, 5]. Micro-terrain in complex environments can cause changes in certain meteorological factors, leading to small-scale micro-meteorological transformations in the near-surface atmosphere that are challenging to identify through macro atmospheric parameter characteristics.

The micro-terrain conceals abundant wind energy resources and poses extreme weather risks, making it increasingly important to identify features of micro-terrain for the rapidly developing globalized power grid. Operational data indicates that most sections where galloping, icing, and wind deflection failures have occurred in the past decades are located within micro-topographic regions. Therefore, its modeling and analysis method is essential for sustainable wind power generation and ultra-high voltage transmission development.

Currently, within the realm of research about transmission line hazards, there are two primary categories of research methodologies. The first category entails research grounded in statistical modeling. In the literature, [6] and [7] employ a statistical model that relies on line failure rates and weather modeling to evaluate the risk associated with transmission lines in the context of meteorological hazards. However, this approach falls short in accounting for the nuanced influence of micro-topographic factors on anomalies and exhibits a relatively modest level of resolution, rendering it more suitable for broad-scale analyses. Turning to [8], it delineates ice-covered areas within the grid using meteorological data. Nevertheless, due to a dearth of substantial ice-related data, it relies solely on fundamental meteorological data to assess the impact on ice cover thickness. As for [9], it employs the annual average daily distribution map of freezing rain to depict the distribution of ice-covered areas. However, this study is limited by the number and distribution of freezing rain observation points, preventing the creation of comprehensive nationwide statistics. Lastly, [10] establishes an efficient early warning model of wind hazards, incorporating simplified micro-topographic wind speed correction coefficients, 24-hour weather forecasts, and transmission line tower data. However, for computational efficiency, these wind speed correction coefficients have been engineered for simplification, rendering them more suitable for large-scale wind hazard early warning systems. [11] provides a robust analysis for the design and reliability assessment of high-voltage transmission lines in the mountainous terrain of Canada by integrating advanced statistical methods to estimate wind speed, temperature, and precipitation rates. The empirical equation-derived ice accretion predictions form the basis for establishing distribution models. However, the model's consideration of the actual complex terrain is limited, with the exception of altitude, indicating a potential area for further refinement.

The second category of methods relies on numerical simulation. [2] employs GIS information modeling for direct target siting, combining CFD simulations validated by wind tunnel experiments with meteorological measurements to optimize wind turbine placement. [12] focuses on actual transmission lines, proposing a rational jumper calculation model and comparing wind deflection in flat areas and specific mountainous terrains. [13] directly models the terrain around accident sites, conducting LES to analyze jumper wind deflection under the combined influence of typhoons and micro-topographic mountainous terrain. [14] also employs GIS information modeling for direct target siting, creating a 1:1300 terrain model and studying average and turbulent wind characteristics through numerical simulation and wind tunnel experiments. [15] contends that wind power plants are crucial renewable energy resources characterized by low generation costs, simple infrastructure, and environmental advantages. With the emergence of advanced solid-state power devices and converters, there is now the potential to transmit substantial amounts of renewable energy to the main electrical grids. Accurate and reliable wind speed predictions are expected to facilitate the efficient utilization of renewable energy in future grids, forming a crucial foundation for future development. [16] explores the non-Gaussian characteristics of wind speed in complex terrain by the LES method. These findings offer valuable insights for assessing extreme wind loads on structures in complex terrain, underscoring the importance of considering non-Gaussian wind characteristics in wind-resistant designs, pointing towards future directions in researching complex wind fields. These methods are primarily used for analyzing known fault lines, characterized by high model accuracy but substantial computational resource demands, making them unsuitable for large-scale computations. Moreover, they do not comprehensively consider the complex effects of micro-topography and meteorological factors. Currently, micro-terrain identification primarily relies on on-site surveys by design personnel, resulting in suboptimal recognition efficiency. Therefore, it is prudent to introduce a micro-terrain recognition model for pinpointing target locations and mitigating computational burdens.

As GIS technology continues to integrate further into the field of electrical engineering, enhancing its comprehensive capability in handling spatial and attribute data [17-20], the achievement of micro-terrain recognition becomes imperative. A profound exploration of the geographic and meteorological characteristics of small-scale terrain and microclimatic regions, as well as their impact on transmission lines, is warranted.

Terrain classification methods are essential tools in landform research, used to extract information about landform features and types from terrain data. Through terrain identification, it becomes possible to gain an in-depth understanding of the spatial distribution of land surface forms, their evolutionary processes, and the relationship between landforms and the environment. [19, 21] constructed a convolutional neural network model for the automatic classification of micro-terrain in raster DEM, enhancing the automation level of classification. They proposed a combination of terrain features, including terrain position index, slope, relative elevation, and water body distance, specifically tailored for micro-terrain transmission lines. [22] employed DEM image textures and convolutional neural networks for deep learning, verifying the effectiveness of texture features in landform classification. Their research findings serve as important references for improving and optimizing landform classification methods.

These studies mainly employ machine learning methods to learn from relevant samples, yielding certain achievements. However, these models often lack interpretability, and the physical meanings of terrain attributes and features remain unclear. Moreover, they demand high-quality and large quantities of samples.

Micro-terrain typically induces small-scale climate characteristics in the near-surface atmospheric layer and at the ground level. These localized climate features are often manifested in the numerical values of specific meteorological factors, without significantly altering the weather and climate characteristics determined by large-scale processes. To address various transmission line disasters in micro-topographic regions, researchers primarily focus on meteorological factors such as temperature, humidity, and wind speed. They employ methods such as statistical models [11], empirical formulas [23], and simulation calculations [23] to establish the relationship between terrain and microclimate. Micro-terrain and microclimate are closely interconnected, but most existing research tends to separate the study of micro-terrain from that of microclimate.

Based on the literature analysis mentioned earlier, there is currently a deficiency in effective methods for analyzing disasters on transmission lines within the saddle micro-terrain environment. Describing the geographical attributes of saddle micro-terrain proves challenging, and there is a lack of viable identification methods beyond manual recognition. Additionally, the scarcity of observational data for transmission lines in the relevant regions compounds the difficulties.

Consequently, this study is aimed at investigating analytical and computational methods specific to the analysis of common saddle-shaped micro-terrain found in mountainous regions. The primary contributions of this research can be summarized as follows:

(1) The proposal of a classification and identification method for these terrains by extracting topographical features distinctive to various saddle micro-terrains. This method facilitates the identification of micro-terrain locations encountered along extended transmission lines, thereby narrowing the scope of disaster analysis and reducing computational demands.

(2) Accomplishing simplified modeling based on the geographical attributes of saddle-shaped micro-terrain. This approach accurately characterizes wind field features associated with diverse saddle micro-terrains and evaluates their impact on transmission lines. It circumvents inherent sample dependency issues present in statistical modeling approaches and general limitations associated with direct modeling from DEM data.

(3) Introduction of a multimodal analysis method that combines meteorological data from meteorological agencies with transmission line sag models. This integrated approach comprehensively considers the catenary characteristics of transmission lines under micro-terrain conditions and meteorological features. It contributes to the refinement of transmission line designs in saddle-shaped micro-terrain environments.

2 Saddle Micro-terrain Identification

Complex mountain ranges exhibit intricate patterns resembling leaf textures, with numerous large ranges branching out from a main range, further dividing into secondary ranges. Saddle-type micro-terrain is predominantly found in mountainous stretches, characterized by mountain ridgelines and noticeable saddle-like depressions.

2.1 **Typical saddle micro-topographic features**

Fig.1(a) and Fig.1(b) illustrate two common types of saddle micro-terrain. When transmission lines traverse these mountainous regions, they tend to avoid crossing the ridgelines of major mountain ranges to minimize the impact of high-altitude crosswinds. Consequently, they often intersect with secondary mountain range groups. The speed-up effect occurring within these depressions amidst narrow secondary ranges causes the airflow to be accelerated, resulting in their recognition as saddle terrains, as depicted in Fig.1(c). To effectively classify and identify saddle micro-terrain, this study employs hydrological analysis and surface calculation methods commonly used in geography. These techniques facilitate the extraction of various terrain features and elements, enabling a comprehensive understanding of the saddle terrain characteristics.

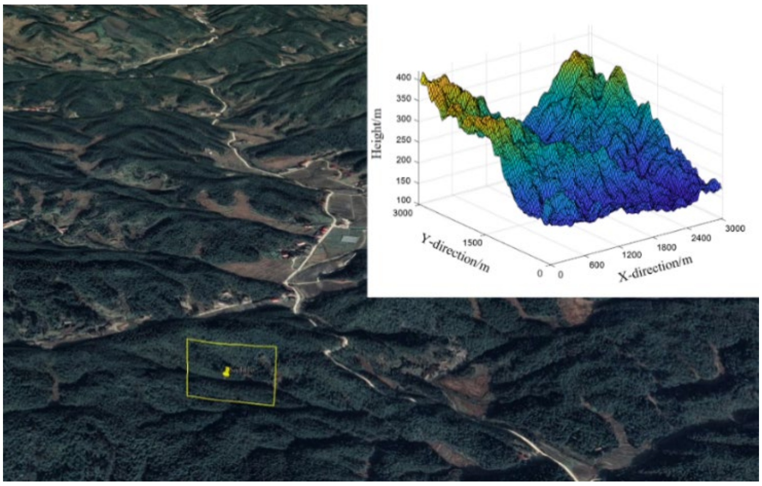

(a) Mountain range saddle

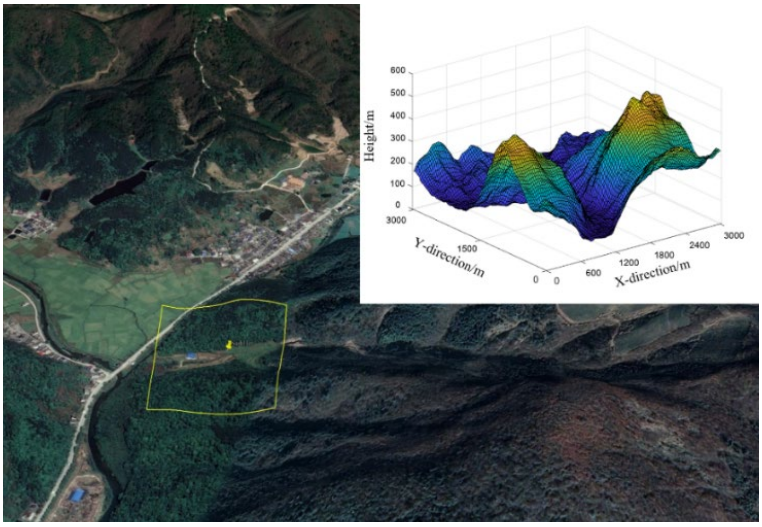

(b) Dual-mountain saddle

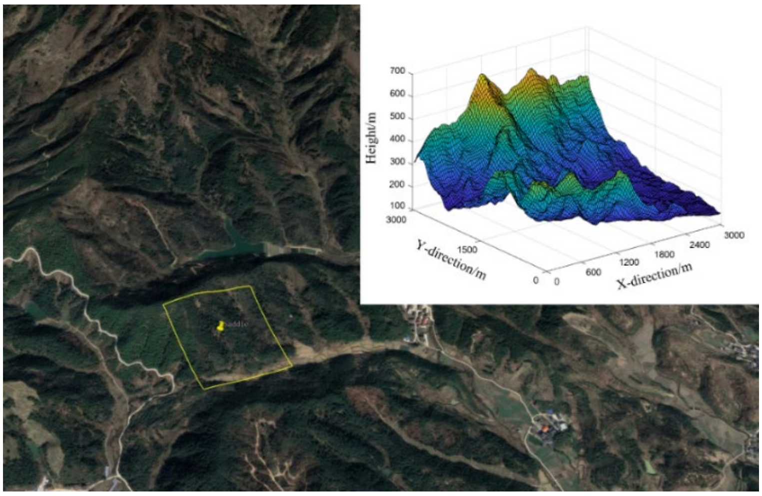

(c) Secondary mountain range saddle

Fig.1 Typical saddle reality view with digital elevation topographic map

2.2 **Terrain Models Simplified by Terrain Factors**

The numerical computational model based on fluid mechanics is closely related to the terrain characteristics of micro-terrain. Its geometric parameters need to be obtained from the terrain information embedded in the DEM. Terrain information can be categorized into two primary categories: terrain surface parameters and terrain morphological characteristics. Terrain surface parameters, including slope, aspect, and curvature, exhibit clear mathematical expressions and can be directly measured using DEM. Conversely, terrain morphological features, although defined clearly, involve some level of ambiguity in their boundary conditions, making them less suitable for mathematical representation. These features are extracted by leveraging the spatial characteristics and interrelationships within surface morphology, resulting in the identification of terrain feature points, terrain feature lines, hydrological elements, and other relevant attributes. Some of the parameters commonly used in mountain modeling are shown in Fig.2:

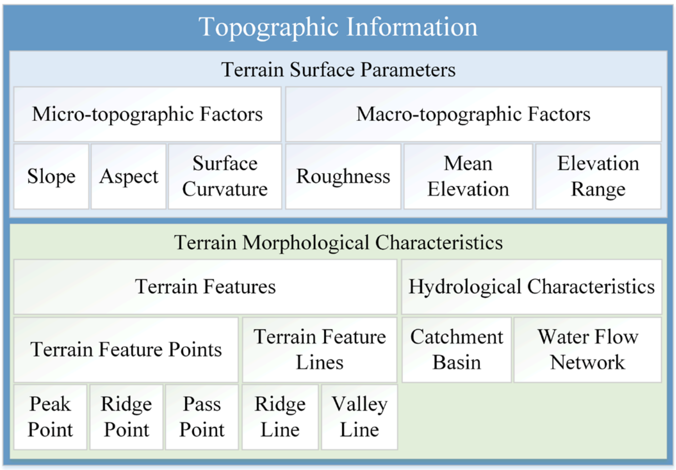

Fig.2 Topographic information classification

In the classification of landform morphology types, elevation plays a dominant role, while slope and aspect are fundamental parameters for surface morphology. However, the aspect is directional, which may result in the same aspect values for plains and mountains, hindering landform morphology classification. On the other hand, ridges and valleys offer straightforward and significant topographic information, aiding landform classification. Additionally, ridgelines and valley lines serve as critical boundaries for elevation changes, essential for micro-terrain identifications. Therefore, this study extracts slope, elevation change, ridgelines, valley lines, and saddle points, utilizing topographic feature lines to create a saddle micro-topography feature section within a geographic model. This model simplifies the terrain model and enables the classification of saddle micro-terrain. Furthermore, meteorological parameters and a transmission line sag model were introduced to construct a multimodal calculation model. The overall technical roadmap is shown in Fig.3

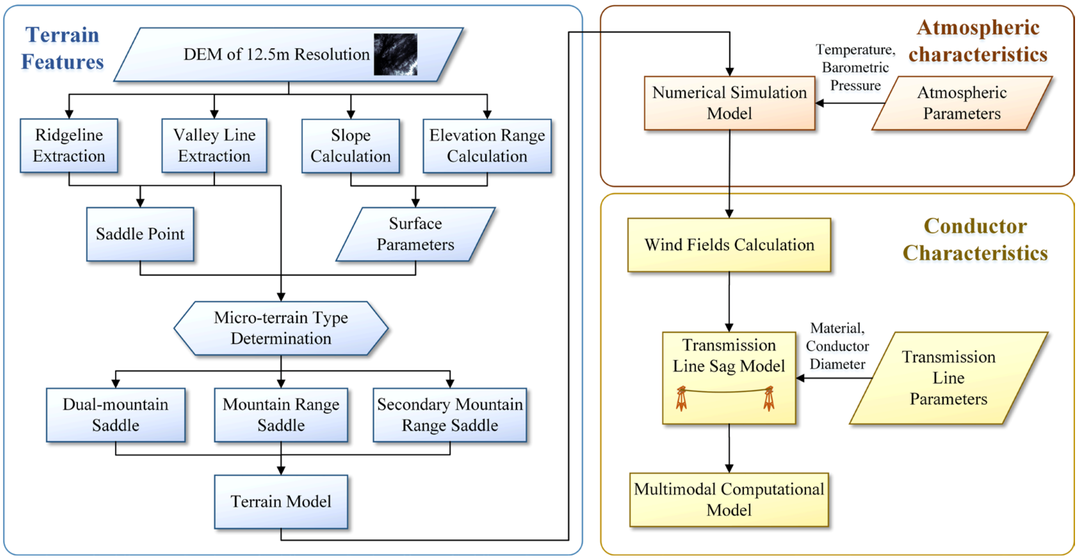

Fig.3 Technology roadmap

In terrain modeling, a 3 km×3 km area is chosen, and its DEM elevation matrix is obtained from publicly available data from ASF DAAC. The maximum slope algorithm [26] is employed to extract fundamental terrain parameters such as mountain peaks, slopes, and terrain roughness. Using hydrological analysis [27], the matrix undergoes depression filling and plain elevation, resulting in a depression-free elevation matrix. This process calculates the flow direction matrix and accumulates flow accumulation along the flow direction to construct a watershed tree. Consequently, this enables the connection of confluence points to obtain valley lines, and similarly, ridge lines can be obtained through reverse terrain analysis.

For micro-terrain analysis, two feature parameters, flow accumulation, and terrain roughness, are considered as criteria for classifying ridge lines into primary and secondary ridges [28]. Based on this hierarchy, the identification of saddle micro-terrain is possible, determining terrain feature points a and b (mountain peaks), and identifying saddle point P where the valley line intersects the horizontal projection of line segment ab. This preliminary assessment indicates the presence of saddle micro-terrain in the area.

Further subdivision involves categorizing it as a dual-mountain saddle if only mountain peaks exist without continuous long ridges. If only primary ridge lines are present in the region, it is classified as a mountain range saddle. On the other hand, if secondary ridge lines exist on both sides of the saddle point, it is classified as a secondary mountain range saddle. These categories exhibit similar characteristic cross-sections. As an example, the contour lines and characteristic cross-sections for secondary mountain range saddles are shown in Fig.4 below.

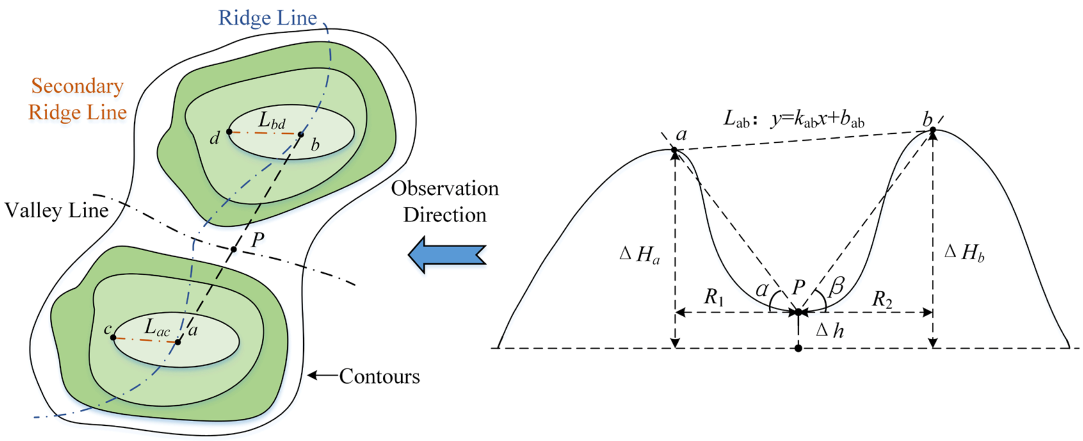

Fig.4 Schematic diagrams of the mathematical definition of typical micro-terrains

Where ΔH_a , ΔH_b and Δh indicate the vertical projection distance from the horizontal plane to the feature point (m); R_1 and R_2 denote the horizontal projection distance between the saddle point P and the feature point on both sides (m); $\tan\alpha$ and $\tan\beta$ denotes the ratio of slope on both sides. L_{ac} and L_{bd} indicate the length of secondary ridge line.

3 Multimodal computational model

Numerical simulations are conducted through FLUENT. In wind engineering, the air is typically turbulent, necessitating the system to comply with additional turbulent transport equations.

In the context of a continuous fluid medium, the motion of mass follows the principle of mass conservation, which means that the net mass inflow into each face of the fluid element per unit time equals the increase in mass flow within the same element during that time interval. This conservation can be expressed mathematically through a continuum equation [29]:

$$\frac{\partial \rho}{\partial t}+\sum_{i=1}^{3}\frac{\partial \rho u_i}{\partial x_i}=0 \quad (1)$$

where $u_i\left(i=1,2,3\right)$ is the velocity component of the velocity function of a given spatial point in the x, y, and z directions, respectively, ρ represents the air density.

Any macroscopic low-velocity moving matter must satisfy Newton's second law, and in fluid dynamics, the conservation of momentum equation is obtained for a fixed volume element or microcluster of mass ρdV :

$$\rho dV\frac{Du_i}{Dt}=\rho dVf_i+\frac{\partial \sigma_{ij}}{\partial x_j}dV \quad (2)$$

where f_i is force acting on a unit fluid mass, σ_{ij} is internal stress of volume element dV

As u_i is the velocity function of a given spatial point, which is a function of both time t and the spatial coordinates x_i . Therefore, $u_i=u_i\left(x_1,x_2,x_3,t\right)$ derivative with respect to time is:

$$\frac{Du_i}{Dt}=\frac{\partial u_i}{\partial t}+\frac{\partial u_i u_j}{\partial x_j} \quad (3)$$

In general, for incompressible fluids such as air moving at low velocity at room temperature, the volume expansion rate is 1.01. According to the above equation and the assumptions, the simplified continuity equation and the equation of motion can be derived as follows:

$$\sum_{i=1}^{3}\frac{\partial u_i}{\partial x_i}=0 \quad (4)$$

$$\rho\frac{\partial u_i}{\partial t}+\rho u_j\frac{\partial u_i}{\partial x_j}=\rho f_i-\frac{\partial p}{\partial x_i}+\mu\frac{\partial}{\partial x_j}\left(\frac{\partial u_i}{\partial x_j}\right) \quad (5)$$

where $\mu\left(N\cdot s/m^2\right)$ is the fluid dynamic viscosity coefficient.

This study employs the Realizable *k*-*ε* two-equation model to simulate the atmospheric boundary layer flow, which is effective in handling flows with high strain rates and large flow line curvatures. The velocity-pressure coupling equations are solved using the SIMPLEC method, while the momentum, turbulent kinetic energy, and turbulent kinetic energy dissipation rate equations are discretized using the second-order upwind scheme for the nonlinear convective terms. The simulation is deemed to have reached a steady state when the residuals of k and ε are less than 10^{-4}, which serves as the simulation criterion.

3.1 **Numerical simulation model**

In the study of wind fields within the atmospheric boundary layer, researchers commonly use the outer contour to construct mountain models. However, due to the complexity and variability of actual mountain shapes, the previously constructed characteristic cross-sections are used as the source of parameters for the outer contour equation to recreate the saddle micro-terrain. The main body can be approximated as composed of stretched segments of the mountain's outer contour with a certain length. At the extension of the mountain range, a combination of three-dimensional models using the rotation and lofting of partial contour lines is employed to construct the numerical computational model.

The outer contour of mountains can be classified into various types, including Sinusoidal, Cosine, Bell, and Gaussian types. The Cosine type more closely approximates the majority of mountain outer contours, and thus, this paper employs cosine-type modeling for the general mountain outer contour, with the following expressions in Table 1 [30]:

Table 1 Outer contour of mountains

Hill shape	Analytic form
Cosine squared	$z=\begin{cases}H\cos^2(\pi r/D) & \text{for } \lvert r\rvert\le D/2\\ 0 & \text{otherwise}\end{cases}$

Where H denotes the height of the mountain and D denotes the diameter of the mountain.

The schematic diagrams of the dual-mountain saddle and mountain range saddle are shown in Fig.5 (a) and (b) respectively, where W represents the inter-mountain distance, and L represents the length of the ridgeline. However, due to the difference in elevation between the secondary ridgeline and the mountain peak, the numerical model for the secondary mountain range saddle shown in Fig.5 (c) introduces an additional parameter γ, which represents the angle of the mountain flank uplift, and L represents the length of the secondary ridgeline, as shown in the diagram.

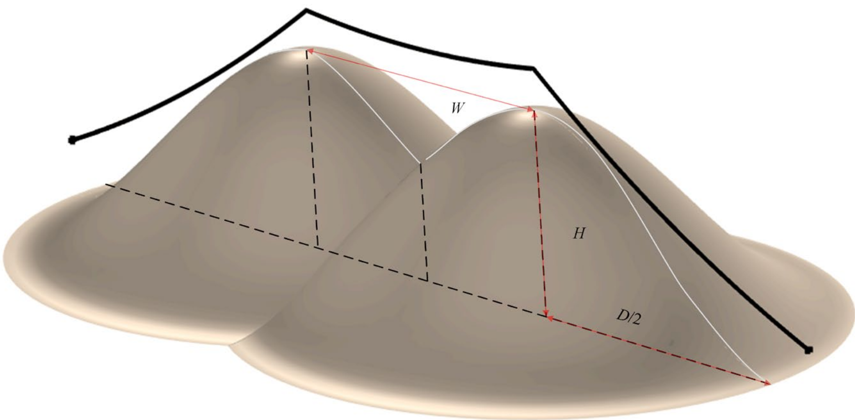

(a) Dual-mountain saddle

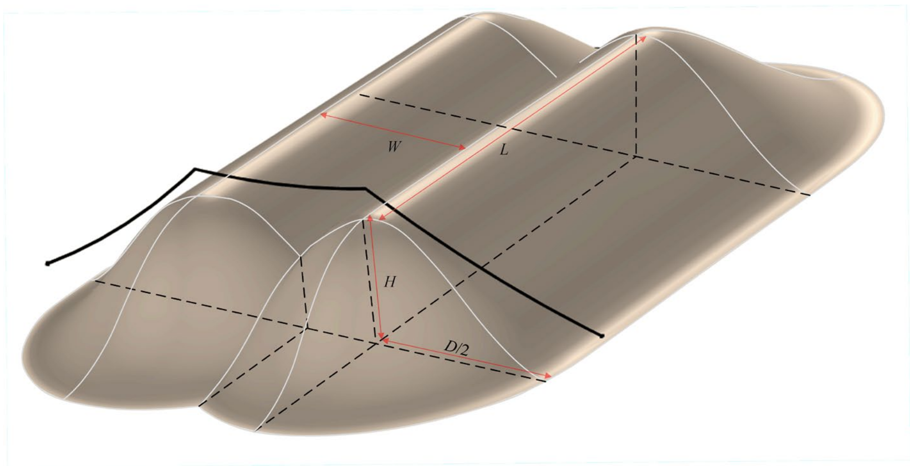

(b) Mountain range saddle

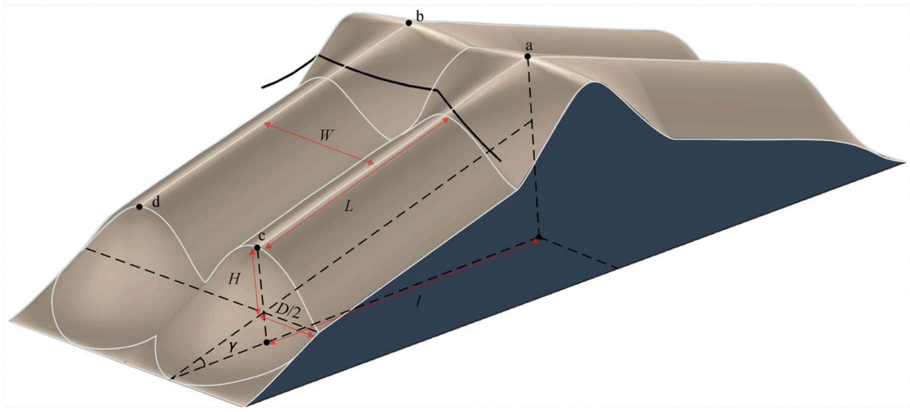

(c) Secondary mountain range saddle

Fig.5 Simulation model

As the influence of topography on the wind field is primarily considered at the micro-topographic scale, the modeling parameters are only related to the geographic elements extracted within the micro-terrain, and the main modeling parameters are transformed as follows:

$$H = \max\left(H_a, H_b\right) \quad (6)$$

$$D = 2H/\tan\alpha \quad (7)$$

$$\tan\alpha = \left(H - h\right)/R \quad (8)$$

$$W = R_1 + R_2 \quad (9)$$

$$L = \max\left(L_a, L_b\right) \quad (10)$$

In particular, for the secondary mountain range saddle model, there are

$$\tan\gamma = \left(\Delta H_a - \Delta H_c\right)/l \quad (11)$$

$$L = l/\cos\gamma - D/2 \quad (12)$$

To facilitate physical modeling, a set of typical parameters is selected shown in Table 2 of micro-terrain based on actual cases and verify the influence of micro-terrain through simulation calculations to verify the influence of micro-topographic areas on the wind field distribution of transmission corridors.

Table 2 Typical saddle micro-terrain parameters table

Saddle Type	D(m)	H(m)	W(m)	L(m)	γ(°)
Dual-mountain saddle			150		
Mountain range saddle	300	100	150	300	
Secondary mountain range saddle			200	300	10

3.2 **Simulation condition setting**

The calculation domain for saddle models should be 7 and 8 times the characteristic width and height of the mountain, respectively. For the secondary mountain range saddle, any symmetric section can be chosen, with a width and height of 1 time and 20 times the characteristic width and height of the mountain, respectively. This study utilized structured meshing with C-cut and O-cut techniques to enhance mesh quality and prevent small-angle mesh appearance. The model mesh quality was maintained above 0.4, while the minimum angle was held at or above 36°.

The velocity entrance is specified as the boundary condition for the flow field entrance. The entrance is located in a mountainous area, classified as a Class B landform according to China's standard. The wind velocity entrance profile is adjusted using equation (13) to ensure an equilibrium boundary layer flow field. To model turbulence at the entrance, the profile of turbulent kinetic energy k and dissipation rate ε is obtained from the Japanese building industry. The parameters used for the turbulent kinetic energy and dissipation rate profiles at the entrance are as follows [31].

$$U(z) = U_r\left(\frac{z}{z_r}\right)^{\alpha} \quad (13)$$

$$k(z) = 0.5[U(z)I(z)]^2 \quad (14)$$

$$\varepsilon(z) = \frac{qC_u^{0.75}k(z)^{1.5}}{KL_u} \quad (15)$$

where z_r is the reference height, U_r is the wind speed at the reference height, α is the mean wind profile index, $I(z)$ is the turbulence degree, C_u is the empirical constant, K is the Carmen constant, and L_u is the turbulence integration scale; α=0.15, C_u=0.09, K=0.42 for Class B landscapes, L_u as well as I(z) are taken according to the Japanese standard. The inlet parameters are defined by the user-defined function.

In general, CFD simulations often use default atmospheric conditions while neglecting the influence of local topography. However, micro-topography significantly affects local meteorological environments, necessitating the correction of microclimate inputs. Notably, average temperature and atmospheric pressure are strongly correlated with the elevation of measurement points. Therefore, this study utilizes meteorological data publicly available from the National Meteorological Science Data Center for meteorological parameter calibration and configuration [32].

$$k_a^{'} = e^{-H/8150} \quad (16)$$

$$Z = \sum_{i=1}^{n} \frac{Z_i}{d_i^p} \Big/ \sum_{i=1}^{n} d_i^{-p} \quad (17)$$

In the equation: $k_a^{'}$ is relative barometric pressure, H is elevation. Z represents the estimated temperature in degrees Celsius, n is the number of observation stations, Z_i is the actual temperature measurement at observation point i in degrees Celsius, d_i is the Euclidean distance between the interpolation point and observation point i, and p is the power of the Euclidean distance. p = 2 in this study.

3.3 **Transmission line sag model**

Under the known distribution of wind field in the saddle micro-terrain, determining the sag curve of the transmission line in the saddle and the tower location allows us to obtain the along-line wind speeds of the transmission line.

The line suspended between the two towers is not straight under the influence of its weight. To faithfully represent the actual conditions of the line, it is necessary to calculate the sag curve between the towers. There are various methods for calculating the sag curve of the conductor, and the catenary method [33] is commonly used in engineering to calculate the sag curve of equidistant tower lines, which is relatively straightforward. However, calculating the sag curve of non-equidistant tower lines is relatively complex. In this study, the unit conductor between towers is treated as a truss unit subjected only to axial forces, and a truss model is adopted to calculate the sag curve of the line between towers.

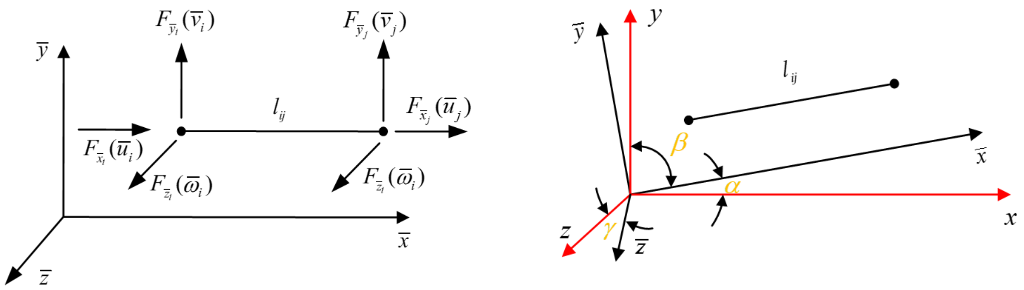

(a) Unit line force analysis (b) Coordinate transformation

Fig.6 Schematic diagram of unit line force

Selected the unit line axial direction as the positive direction of $\bar{x}$, the normal direction as the unit line positive direction of $\bar{y}$ and $\bar{z}$, and they are perpendicular to each other, $F_{\bar{x}_i}$, $F_{\bar{y}_i}$, $F_{\bar{z}_i}$ denote the left node in the three directions of the force component respectively, and $F_{\bar{x}_j}$, $F_{\bar{y}_j}$, $F_{\bar{z}_j}$ denote the right node in the three directions of the force component respectively, the same reason, $\bar{u}_i$, $\bar{v}_i$, $\bar{\omega}_i$, $\bar{u}_i$, $\bar{v}_i$, $\bar{\omega}_j$ denote the left and right side of the node in the three directions of the displacement component respectively, as shown in Fig.6(a), then the line node force vector and displacement vectors exist in the equation [34]:

$$\{\overline{F}\}_{\mathrm{e}} = \{F_{\overline{x}i} \quad F_{\overline{y}i} \quad F_{\overline{z}i} \quad F_{\overline{x}j} \quad F_{\overline{y}j} \quad F_{\overline{z}j}\} \quad (18)$$

$$\{\overline{\delta}\}_{\mathrm{e}} = \{\overline{u}_i \quad \overline{v}_i \quad \overline{\omega}_i \quad \overline{u}_j \quad \overline{v}_j \quad \overline{\omega}_j\} \quad (19)$$

there exists an equation between $\{\overline{F}\}_{\mathrm{e}}$ and $\{\overline{\delta}\}_{\mathrm{e}}$:

$$\{\overline{F}\}_{\mathrm{e}} = [\overline{K}]_{\mathrm{e}}\{\overline{\delta}\}_{\mathrm{e}} \quad (20)$$

where $[\overline{K}]_{\mathrm{e}}$ is the unit stiffness matrix in this coordinate system:

$$[\overline{K}]_{\mathrm{e}} = \frac{EA}{l_{ij}}\begin{bmatrix} 1 & 0 & 0 & -1 & 0 & 0 \\ 0 & 0 & 0 & 0 & 0 & 0 \\ 0 & 0 & 0 & 0 & 0 & 0 \\ -1 & 0 & 0 & 1 & 0 & 0 \\ 0 & 0 & 0 & 0 & 0 & 0 \\ 0 & 0 & 0 & 0 & 0 & 0 \end{bmatrix} \quad (21)$$

Where E is Young's modulus, A is the cross-sectional area of the conductor, and l_{ij} is the unit conductor length. To facilitate the superposition of the unit line nodal forces and displacements in the subsequent structural analysis, the unit line coordinate system is transformed into a unified coordinate system through a coordinate transformation as presented in Fig.8(b), and the cosines between the unit line and the x, y, and z axes of the unified coordinate system are l, m, and n. The unit stiffness matrix in the unified coordinate system is:

$$[K]_{\mathrm{e}} = [T]\{\overline{K}\}_{\mathrm{e}}[T]^T = \frac{EA}{l_{ij}}\begin{bmatrix} l^2 & lm & ln & -l^2 & -lm & -ln \\ lm & m^2 & mn & -lm & -m^2 & -mn \\ ln & mn & n^2 & -ln & -mn & -n^2 \\ -l^2 & -lm & -ln & l^2 & lm & ln \\ -lm & -m^2 & -mn & lm & m^2 & mn \\ -ln & -mn & -n^2 & ln & mn & n^2 \end{bmatrix} \quad (22)$$

After establishing the stiffness matrix of the individual conductor, the overall stiffness matrix is constructed based on deformation compatibility and the balance of internal and external forces at the nodes. The overall stiffness matrix is singular and cannot be solved directly. It requires the specification of a displacement elimination matrix to remove singularity and enable the solution. In this study, the displacement at both supporting points is specified as 0.0025 times the length of the conductor. The conductor has a diameter of 26.82 mm, a weight of approximately 1349 kg per kilometer, and a cross-sectional area of 425.24mm^2, resulting in a density of 3174kg/m^3. The Young's modulus is set to 60 GPa. Under the influence of gravity, the sag curves of the conductor between equidistant and non-equidistant towers are shown in the following Fig.7.

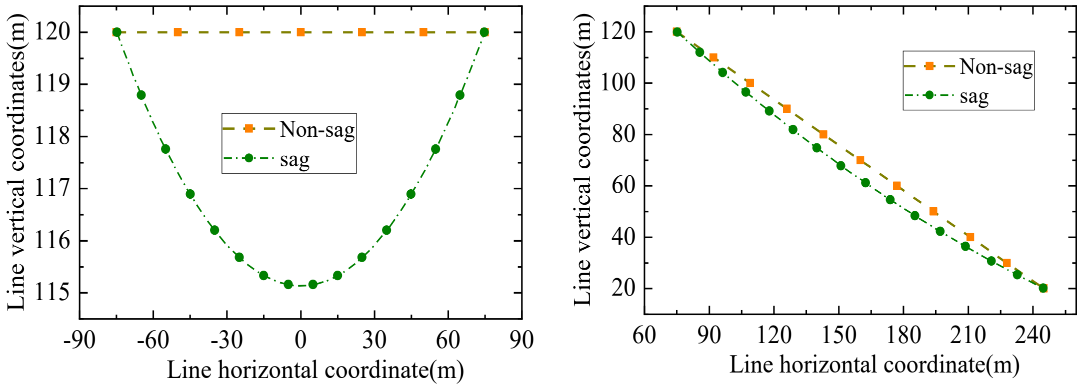

(a) Sag curve of equivalent height tower (b) Sag curve of non-equivalent height tower

Fig.7 Truss model calculation line sag curve of transmission line

4 Analysis and experimental validation

4.1 Characterization of wind lord in micro-terrain

According to the description of the ice cover survey protocol [35], the growth of ice cover is closely related to wind, which in turn is closely related to topography. In the process of airflow movement, the ups and downs of the terrain lead to the diversion, diffusion and concentration of airflow. In addition, wind speed is the environmental factor that is most significantly affected by topographic features, and the data related to wind speed are mainly used to standardize the various protocols. Based on the wind field calculations under micro-terrain, the influence on the wind load of the transmission line can be determined. The LGJ-400/35 conductor is widely used within the common voltage levels in China [36, 37], thus chosen as the subject of study. In this research, the wind load on the conductor is obtained by solving the wind pressure distribution on its surface. The wind pressure on the conductor surface has directionality, with the positive direction defined as perpendicular to the conductor surface. In the case where the wind pressure in the X-direction is known, the wind load on the conductor can be calculated using the following equation [31]:

$$F_{\mathrm{wind}} = \int_{l} \frac{\pi d P_{\mathrm{X}}}{360} d\theta = \frac{\pi d}{360} \sum_{i=1}^{n} P_{\mathrm{X}_i} \quad (23)$$

In the equation, F_{wind} represents the wind load per unit length of the conductor, l represents the surface arc of the conductor, and d represents the diameter of the conductor. Taking a wind speed of 5 m/s as an example, the unit wind load on the conductor is 0.93 N/m.

Wind loads of conductors were calculated for a total of 20 wind speeds, with a gradient of 1 m/s, as shown in Fig.8(a). It can be observed that as the wind speed increases, the wind load approximately exhibits exponential growth.

The wind load curves for Class II lines in the three types of saddles generally demonstrate a decrease in wind load as they move away from the high suspension point. However, a specific section closer to the mountain exhibits a distinct pattern, which refer to as the sag region in this study, as illustrated in Fig.8(c). It is revealed in Fig.8(b) that the wind load curve for the sag region in the dual-mountain saddle displays a concave trend. Meanwhile, the wind load variation in the sag region of the secondary mountain range saddle is relatively small, resulting in a bending wind load curve. Conversely, the wind load curve for the sag region of the mountain range saddle shows minimal changes compared to other regions.

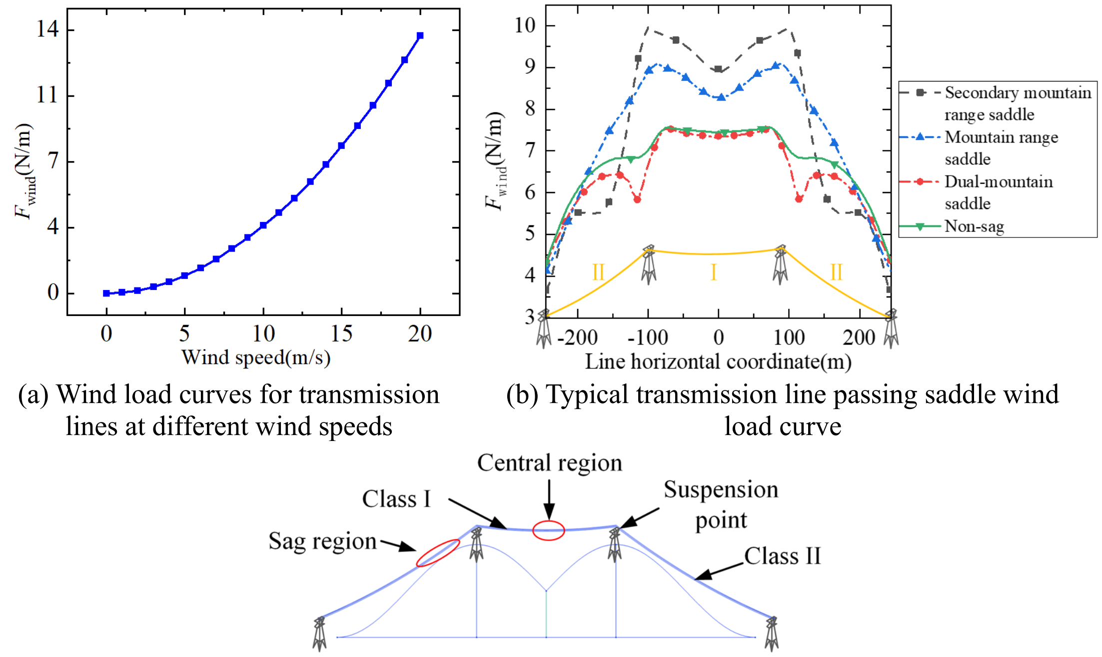

(a) Wind load curves for transmission lines at different wind speeds

(b) Typical transmission line passing saddle wind load curve

(c) Transmission line division description

Fig.8 Wind load curve of the transmission line passing saddle and division of transmission line areas

Using the typical saddles outlined in Table II as a case study, the terrain model was employed to conduct CFD simulations for wind field distribution within the micro-terrain environment. Subsequently, the truss model was used to calculate the sag curve of the transmission line across the saddle point. By utilizing the calculated wind speed distribution results for the saddle point and the unit conductor wind load curves under varying wind speeds, as shown in Fig.8(a), the wind load curve can be obtained for the transmission line in the saddle micro-terrain, as illustrated in Fig.8(b). The solid green line in Fig.8(b) represents the wind load curve of the dual-mountain saddle transmission line without sag (straight line). Comparing it with the wind load curve of the dual-mountain saddle transmission line with sag, it can be observed that the presence of sag influences the line loads differently for the two types.

For Class I lines (located within the saddle), sag results in approximately a 2% reduction in wind load within the central region. Conversely, for Class II lines (outside the saddle), the presence of sag yields a significant difference of up to 17% in the wind load curves between the two lines. This highlights the necessity of considering the actual sag condition when calculating wind loads for transmission lines crossing saddles. Fig.8(b) also depicts the wind load curves of transmission lines traversing outside slopes and saddles.

The peak wind load for all three types of saddle transmission lines is observed at the high suspension points. Among them, the secondary mountain range saddle exhibits the highest peak wind load, followed by the mountain range saddle, while the dual-mountain saddle experiences the lowest wind load intensity. The wind load curves of Class I lines for these saddles display varying levels of concavity in the central region.

At the high suspension point of the secondary mountain range saddle transmission line, the wind load measures 10.03 N/m, whereas the wind load in the central area averages approximately 8.84

N/m, representing a reduction of approximately 13.5%. Similarly, for the mountain range saddle transmission line, the wind load at the high suspension point reaches 9.07 N/m, while the wind load in the central area is around 8.28 N/m, resulting in a reduction of approximately 9.5%. In the case of the dual-mountain saddle, the wind load at the high suspension point reaches approximately 7.56 N/m, while the wind load in the central area averages approximately 7.32 N/m, indicating a reduction of approximately 3.27%. These results indicate that the reduction in wind load is most pronounced in the central region of the secondary mountain range saddle, while the central area of the dual-mountain saddle exhibits the least significant reduction in wind load.

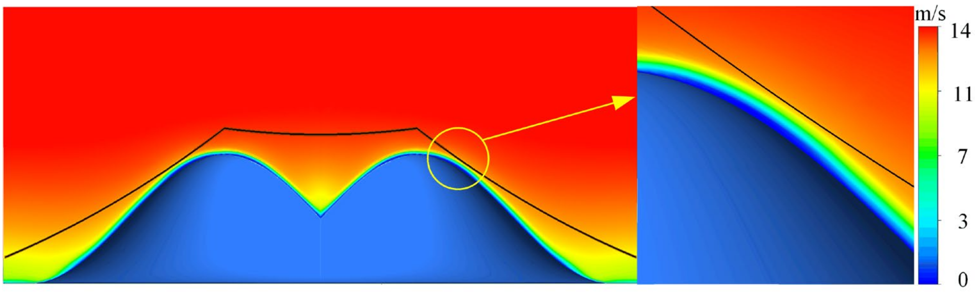

(a) Dual-mountain range saddle

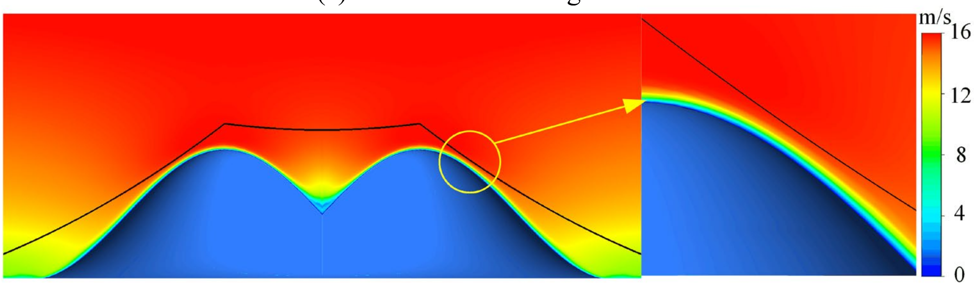

(b) Mountain range saddle

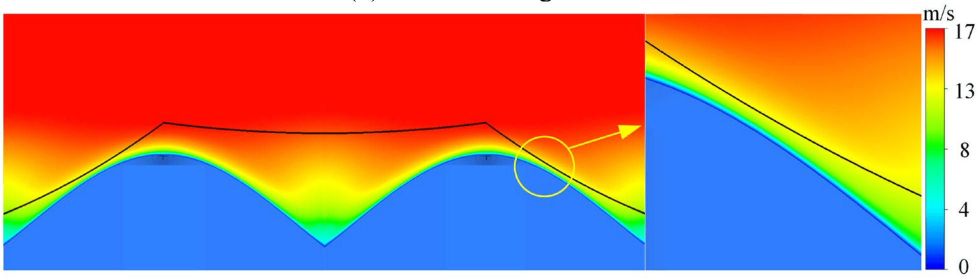

(c) Secondary mountain range saddle

Fig.9 The front view of the cloud map of the wind field on the saddle transmission line

The front views of wind fields for the three types of saddles is depicted in Fig.9. From Fig.9(a), it was observed that in the case of the dual-mountain range saddle and Class II lines, the sag region extends into the boundary layer of the mountain. This spatial arrangement results in a certain distance between adjacent lines and the mountain boundary layer. As the transmission line departs from the lowest point of the sag region, the wind load magnitude increases, leading to a concave trend in the wind load curve within the sag region. In Fig.9(b), it was evident that the sag region of the mountain range saddle does not extend into the mountain's boundary layer. Consequently, there is no significant difference in wind load between the sag region and adjacent regions of the transmission line. This leads to a relatively consistent trend in the wind load curve. Considering the symmetric nature of the secondary mountain range saddle along the direction of the mountain ridge, Class II lines extend from the mountain peak to the bottom area of the saddle, rather than the mountain's base. Fig.9(c) shows that in the case of the secondary mountain range saddle and Class

II lines, the sag region extends into the boundary layer of the mountain. Notably, the lower portion of the sag region remains within the mountain's boundary layer until the line reaches the bottom of the saddle. As a result, after leaving the sag region, the wind load on the line does not undergo significant changes. The wind load curve within the sag region exhibits a bending trend.

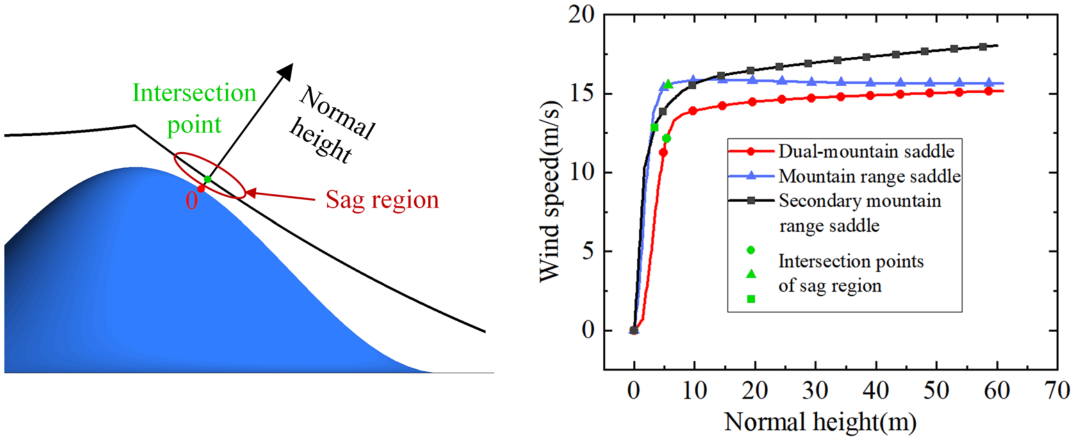

(a) Schematic diagram of the normal height (b) Normal height wind speed profile

Fig.10 Normal wind speed profile in the sag region of the transmission line

Fig.10(a) and (b) illustrate wind speed variation profiles at normal heights in the sag region. Notably, Fig.10(b) reveals a boundary for mountain boundary layer winds. Below the boundary layer height, wind speeds at secondary mountain range saddles, mountain range saddles, and dual-mountain saddles all rapidly increase with normal height, with average growth rates of 4.78, 4.33, and 3.25, respectively. Above the boundary layer height, wind speeds at secondary mountain range saddles and dual-mountain saddles gradually increase with normal height, with reduced average growth rates of 0.22 and 0.09. Wind speeds at mountain range saddles exhibit an average growth rate of less than 0.05, indicating minimal variation with normal height. While the sag curves and mountain profiles for dual-mountain and mountain range saddles transmission lines are similar, their wind load curve trends differ due to distinct wind field distributions. Comparing wind speed profiles at normal heights for saddles, it is evident that the boundary layer at mountain range saddles is thinner, with the intersection point's wind speed growth rate at only 0.18, resulting in relatively stable wind loads. In contrast, the intersection points for secondary mountain range saddles and dual-mountain saddles fall within the boundary layer, with wind speed growth rates of 0.97 and 1.53, indicating substantial non-uniform wind load variations, posing a higher risk of accidents according to current standards.

In the current stage of China, the wind design criteria for mountainous transmission lines are relatively simple, typically using a design standard value of 1.1 times the wind speed on flat terrain. This design approach is overly broad and fails to consider the uneven wind loads on transmission lines caused by saddle micro-terrain. Therefore, further clarification of the influence of saddle terrain parameters on the imbalance of wind loads can provide a basis for differentiated identification of micro-terrain and disaster prevention in mountainous transmission lines.

4.2 **Wind tunnel test verification**

The CQU Open-type Wind Tunnel Laboratory, or CQ-1, is located on the B Campus of Chongqing University. It features an aerodynamic profile measuring 4.4m x 3.4m x 31.2m, and a test section measuring 2.4m (width) x 1.8m (height) x 15m (length). In terms of experimental instrumentation, many tools were used for the experiments including a HFFB, a multi-channel synchronized pressure sensing system, Cobra probes, Laser displacement sensors, and a Dynamic data acquisition system.

To produce a thick boundary layer flow field at a short distance in the wind tunnel test section, a turbulence generation device is required at the entrance of the test section. To better simulate the characteristics of the boundary layer flow field, including turbulence intensity and turbulence integration scale, this study employs the sharp wedge-roughness element technique, as shown in Fig.11.

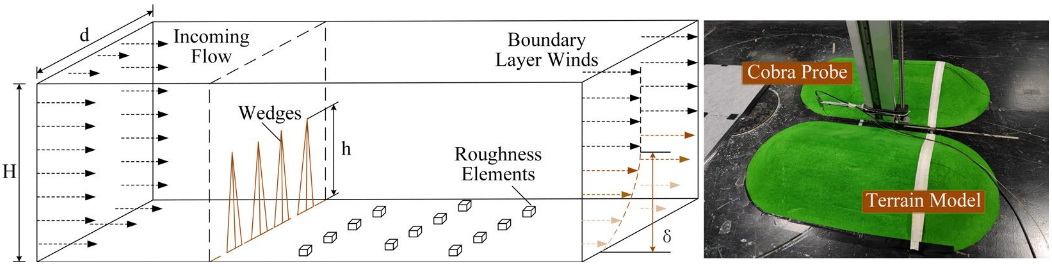

Fig.11 Layout of turbulence generation device in the wind tunnel and saddle terrain model

The usual way to measure the acceleration effect of the mountain on the wind field is dimensionless, using the acceleration ratio *S*, which is defined as [29]:

$$S = \frac{U(z)}{U_0(z)} \quad (24)$$

Where $U(z)$ is the wind speed at z height of the mountain, and $U_0(z)$ indicates the wind speed at z height of the flat land.

Turbulence intensity I is a standard for measuring the degree of airflow velocity fluctuations:

$$I = \frac{u'}{U} \quad (25)$$

Where u' represents the root mean square of turbulence velocity (i.e., the standard deviation of wind speed), and U is the mean velocity.

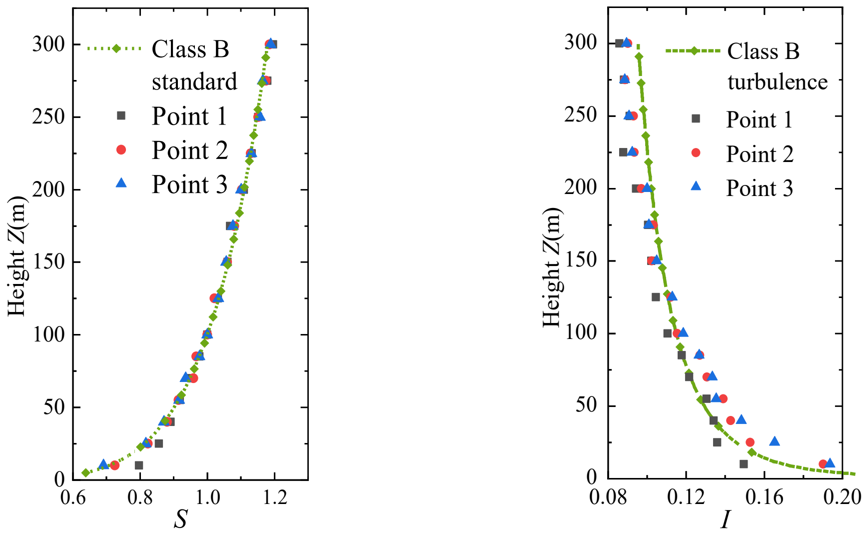

(a) Mean wind profile (b) Turbulence intensity profile

Fig.12 Comparison of wind field measurements with standards

According to the specified criteria for the average wind profile and turbulence profile in Class B terrain [31], when compared to the measured values in a wind tunnel, as shown in Fig.12, the maximum relative error does not exceed 0.1%, it can be considered that the wind tunnel has accurately recreated the wind field in the actual environment.

The acceleration ratio profile of the micro-terrain wind field is shown in Fig.13. The left side is the incoming direction of flow. The findings of the wind tunnel testing have confirmed the CFD calculations for all measurement points, with a substantial alignment between the CFD results and the wind tunnel test results. The error in the valley line indicates that the measured acceleration effect is slightly greater than the simulation result. The primary reason for this discrepancy is that the model's surface is covered with turf, making it smoother compared to other measurement points. As a result, the wind speed measured at this location is not impeded by surface roughness, leading to a higher value than the simulation calculation results. Therefore, it is possible to use the multimodal computational model to analyze the wind field environment for micro-terrain effectively.

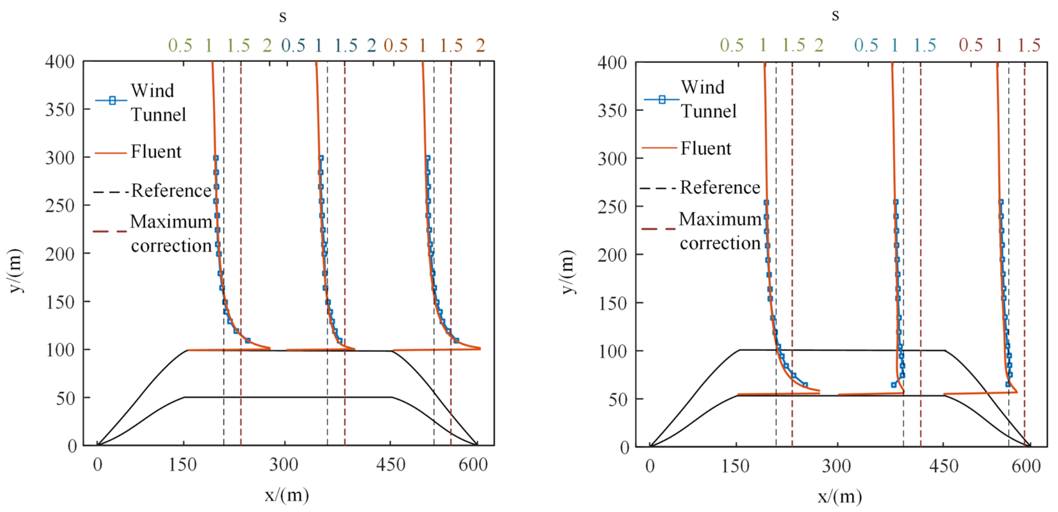

(a) Ridge of the saddle (b) Valley of the saddle

Fig.13 Comparison of measuring point experiment and numerical acceleration ratio

The maximum acceleration ratio occurs at the windward entrance of the saddle terrain, reaching a maximum acceleration ratio of 1.740. As the wind enters the interior of the mountain, the acceleration effect weakens, with a slight resurgence of the acceleration effect at the exit. Generally, the acceleration effect is more pronounced closer to the ridge, but on the windward side, the acceleration effect on the inner side of the saddle terrain may be slightly higher than at the ridge. According to current line survey protocols[35], under operating conditions, the micro-terrain-corrected wind speed for overhead transmission lines is typically 1.2 times the design wind speed, with a maximum corrected wind speed of 1.5 times. If the actual operating wind speed exceeds the corrected wind speed due to the saddle micro-terrain, the ice thickness on the transmission lines influenced by micro-terrain is likely to exceed the design standard, significantly increasing the probability of wind disasters. This study uses the maximum correction as the criterion. Under the saddle micro-terrain, numerical simulation results indicate that the above micro-terrain features exhibit distinct micro-meteorological characteristics, with the wind field at the windward and mountain ridge entrance being the most significantly affected.

5 Conclusion

This study utilizes real case examples of saddle micro-terrain and micro-meteorological conditions to investigate the identification scheme and analysis method based on topographic feature extraction. By considering the geographical and meteorological features and the transmission line sag model under micro-terrain, we analyze the impact of different saddle micro-topographic features on transmission line wind loads. It enhances the computational efficiency and precision of wind field analysis for transmission lines in micro-terrain regions. The following conclusions are drawn from this study:

(1) An identification method for saddle micro-terrain is proposed by comprehensively considering its topographic features and topological structure. The extraction of characteristic terrain elements and parameters from the DEM enables the formation of representative cross-sections for classification purposes. Additionally, a numerical simulation calculation model has been developed based on the parameters of the characteristic sections and outer contour lines.

(2) By equating the conductor unit to a truss unit solely subjected to axial force, the sag curve model of the transmission line has been obtained. The wind field of the saddle terrain, considering typical shape parameters, has been calculated. The wind speed distribution and intervals of the transmission line at the saddle have been derived, with a clear understanding of the line erection method.

(3) By coupling the geographical and meteorological features of micro-terrain with the sag model of transmission lines, a multimodal computational model for long-distance transmission lines under micro-topographic conditions has been established. The wind load on conductors has been calculated for various wind speeds within the wind speed interval of the line. It has been observed that the conductor wind load exhibits an approximately exponential increase with the increment of wind speed.

(4) Class II lines are positioned on the outer side of the saddle, extending from one mountain peak to the outer foothills. The proximity between the line and the mountain is significantly smaller than that of Class I lines, and the line naturally sags, further reducing this distance. The sag region may extend into the boundary layer region of the mountain, where the boundary layer effects caused by the mountain alter the wind load at that specific location. Consequently, the wind load curve pattern within the sag region differs from that of other regions. For lines located inside the saddle, the sag resulted in a reduction of wind loads in the central region of approximately 2%. For lines located outside the saddle, the presence of sag produces a significant difference of up to 17% in the wind load curve between the two lines.

(5) The boundary layer of the mountain range saddle is thinner than the other two types of boundary layer, so the intersection of the line of the mountain range saddle will not intrude into the boundary layer, and the growth rate of the wind speed at this point is only 0.18, and the change of the wind load is relatively more stable, while the intersection of the transmission lines' sag region of the secondary mountain range saddle and the sag region of the dual-mountain saddle falls into the boundary layer, and the growth rate of the wind speed at the intersection is up to 0.97 and 1.53 respectively, and the small change of the elevation difference will bring great uneven wind load, which is more likely to lead to accidents. The numerical simulation results reveal distinctive micro-meteorological characteristics associated with the

mentioned micro-terrain features, particularly showcasing the pronounced impact on the wind field at the windward and mountain ridge entrance.

(6) This approach presents a practical solution by avoiding global calculations for the entire span of transmission lines. Instead, it extracts geographic features and identifies micro-terrain areas for detailed analysis, significantly reducing computational resources and time, thus demonstrating practicality. However, the current use of historical meteorological data limits the analysis to uniform wind conditions, necessitating additional field measurements for more complex scenarios like turbulence and gusts. To achieve even more precise analysis at specific locations, an extensive dataset of field measurements is required. Furthermore, our method solely considers the terrain characteristics of saddle micro-terrain, overlooking various real-world environmental factors such as solar radiation, vegetation, and river distribution. Future research could delve deeper into these aspects for a more comprehensive understanding and improved accuracy.

6 Acknowledgements

The work was carried out with the help of the Arctic Technology and Icing Research Group of the Arctic University of Norway and the Power Research Institute of State Grid Xinjiang Electric Power Co. Ltd. The authors would like to thank Xinjiang Key Laboratory of Extreme Environment Operation and Detection Technology of Power Transmission and Transformation Equipment, whose equipment support made this research possible. This work was undertaken as part of the Norwegian Research Council's INTPART program under Contract No. 309241 and Technical Service Contract No.SGXJDK00GYJS2200045 of the Power Research Institute of State Grid Xinjiang Electric Power Co. Ltd.

7 Reference

[1]. Kumar, R., S.K. Mishra and D.K. Mohanta, Reliability and economics evaluation for generation expansion planning incorporating variability in wind energy sources. Electric Power Systems Research, 2023. 224: p. 109720.

[2]. Hu, W., et al., A novel approach for wind farm micro-siting in complex terrain based on an improved genetic algorithm. ENERGY, 2022. 251.

[3]. Yun-na, W., et al., Macro-site selection of wind/solar hybrid power station based on Ideal Matter-Element Model. International Journal of Electrical Power & Energy Systems, 2013. 50: p. 76-84.

[4]. Zhang, Z., et al., Flashover characteristics and altitude correction of railway insulators at high altitude and polluted areas. Electric Power Systems Research, 2023. 224: p. 109724.

[5]. Shilong, H., et al., Effects of the rainfall rate on corona onset voltage gradient of bundled conductors in alternating current transmission lines in high-altitude areas. Electric Power Systems Research, 2021. 200: p. 107461.

[6]. Wang J., Research on Meteorological Disaster Risk Analysis and Fault Early Warning Methods for Overhead Transmission Lines, 2016, Chongqing University.

[7]. Zhang X. M., Key Technology of Transmission Line Galloping Distribution and Monitoring and Early Warning Based on Multi-Source Spatio-Temporal Data, 2020, Wuhan University.

[8]. Du Z., The Classified according and Severity maps of ice in Chongqing Power Grid, 2011,

Chongqing University.

[9]. Li Q. F., et al, Investigation of Ice-Covered Transmission Lines and Analysis on Transmission Line Failures Caused by Ice-Coating in China. Power System Technology, 2008(09): pp. 33-36.

[10]. Weng S. J., Research of Wind Disaster Early Warning Method for Overhead Transmission Lines, 2015, Chongqing University.

[11]. Davalos, D., J. Chowdhury and H. Hangan, Joint wind and ice hazard for transmission lines in mountainous terrain. Journal of Wind Engineering and Industrial Aerodynamics, 2023. 232.

[12]. Xu H. W., et al, Wind deflection analysis of transmission line jumper under micro-terrain. Journal of Zhejiang University (Engineering Science), 2017. 51(02): pp. 264-272.

[13]. Chen K. J., et al, Wind-induced Flashover Incident Analysis of Jumper Considering the Effect of Typhoon and Mountainous Topography. High Voltage Engineering, 2023. 49(04): pp. 1507-1514.

[14]. Zou, Y.F., et al., Wind Field Characteristics of Complex Terrain Based on Experimental and Numerical Investigation. APPLIED SCIENCES-BASEL, 2022. 12(10).

[15]. Husain, N. and S.M.U. Ali, On Integration of Wind Power into Existing Grids via Modular Multilevel Converter based HVDC Systems. International Journal of Renewable Energy Research, 2020. 10(3): p. 1060-1070.

[16]. Shen, H., et al., Non-Gaussian wind features over complex terrain under atmospheric turbulent boundary layers: A case study. Wind and Structures, 2022. 35(6): p. 419-430.

[17]. Albraheem, L. and L. AlAwlaqi, Geospatial analysis of wind energy plant in Saudi Arabia using a GIS-AHP technique. Energy Reports, 2023. 9: p. 5878-5898.

[18]. Aghaloo, K., et al., Optimal site selection for the solar-wind hybrid renewable energy systems in Bangladesh using an integrated GIS-based BWM-fuzzy logic method. Energy Conversion and Management, 2023. 283: p. 116899.

[19]. Zhou, F. B., et al. Automatic Extraction of Digital Micro Landform for Transmission Lines. Geomatics and Information Science of Wuhan University, 2022(9): pp. 1398-1405.

[20]. Chen, Y. L., et al., A New Method for Automatic Extraction of Ridge and Valley Axes from DEM. Chinese Journal of Image and Graphics, 2001. 6(12): pp. 1230-1234.

[21]. Zhou, F. B., et al. Micro landform classification method of grid DEM based on BP neural network. Geomatics and Information Science of Wuhan University, 2021. 46(08): pp. 1186-1193.

[22]. Xu, Y., et al., Deep learning of DEM image texture for landform classification in the Shandong area , China. Frontiers of Earth Science, 2022. 16(2): p. 352-367.

[23]. Shao, J., et al., Study on windage yaw calculation and real-time warning method of Shanxi power grid considering microclimate and micro-terrain factors. IEEJ Transactions on Electrical and Electronic Engineering, 2018. 13(5): p. 681-688.

[24]. Tang, X., et al., Micro-scale wind resource assessment in complex terrain based on CFD coupled measurement from multiple masts. Applied Energy, 2019. 238: p. 806-815.

[25]. Ha, T., et al., Development of a micro-scale CFD model to predict wind environment on mountainous terrain. Computers and Electronics in Agriculture, 2018. 149: p. 110-120.

[26]. Zhou QM et al, Digital Terrain Analysis. 2006. Science Press.

[27]. Yang, W., et al., Study on urban flood simulation based on a novel model of SWTM coupling D8 flow direction and backflow effect. Journal of Hydrology, 2023. 621: p. 129608.

[28]. Xiong L. Y, Tang G. A. and Yan S. J., DEM-based hierarchical extraction method for mountain saddle points. Surveying and Mapping Science, 2013. 38(2): pp. 181-183.

[29]. Uchida, T. and Y. Ohya, Numerical simulation of atmospheric flow over complex terrain.

JOURNAL OF WIND ENGINEERING AND INDUSTRIAL AERODYNAMICS, 1999. 81: p. 11.

[30]. Weng, W.S., P.A. Taylor and J.L. Walmsley, Guidelines for airflow over complex terrain: model developments. Journal of Wind Engineering and Industrial Aerodynamics, 2000. 86(2-3): p. 169-186.

[31]. China Electric Power Engineering Consultant Group East China Electric Power Design Institute Co. Ltd, Load Code for Overhead Transmission Lines, 2018, National Energy Administration.

[32]. Babak, O. and C.V. Deutsch, Statistical approach to inverse distance interpolation. STOCHASTIC ENVIRONMENTAL RESEARCH AND RISK ASSESSMENT, 2009. 23(5): p. 543-553.

[33]. Wu, Y., et al., A Hybrid Framework Combining Data-Driven and Catenary-Based Methods for Wide-Area Powerline Sag Estimation. ENERGIES, 2022. 15(14).

[34].Standardization, E.C.F., Eurocode 3: Design of steel structures part I, E.C.F. Standardization, E.C.F. Standardization^Editors. 1992.

[35]. China Electric Power Engineering Consultant Group Southwest Electric Power Design Institute Co. Ltd, Protocol for Ice Covering Survey of Overhead Transmission Lines, 2015, National Energy Administration

[36]. Yang, G., et al., Research on load transfer melt-icing technology of transmission lines: Its critical melt-icing thickness and experimental validation. Electric Power Systems Research, 2023. 221.

[37]. Liu, Y., et al., A helical charge simulation based 3-D calculation model for corona loss of AC stranded conductors in the corona cage. AIP ADVANCES, 2018. 8(1).